Sebastian Stein, Theresa Block, Steffen Klenner, Lukas Heletta and Rainer Pöttgen*

Equiatomic iron-based tetrelides *T*FeSi and *T*FeGe (*T* = Zr, Nb, Hf, Ta) – A ^{57}Fe Mössbauer-spectroscopic study

https://doi.org/10.1515/znb-2018-0237
Received November 8, 2018; accepted November 16, 2018

Abstract: The equiatomic iron-silicides *T*FeSi as well as the corresponding germanides *T*FeGe with the electron-poor 4*d* and 5*d* transition metals (*T* = Zr, Nb, Hf, Ta) have been synthesized from the elements by arc-melting. All samples were characterized through their lattice parameters using powder X-ray diffraction (Guinier technique). Four structures were refined from single-crystal X-ray diffractometer data: *a* = 640.16(3), *b* = 393.45(5), *c* = 718.42(6) pm, *Pnma*, 390 F^2 values, 20 parameters, *wR*2 = 0.0294 for ZrFeSi (TiNiSi type), *a* = 719.63(11), *b* = 1119.27(7), *c* = 649.29(7) pm, *Ima*2, 1103 F^2 values, 54 parameters, *wR*2 = 0.0555 for NbFeGe (TiFeSi type), *a* = 655.96(7), *c* = 372.54(4) pm, $P\bar{6}2m$, 251 F^2 values, 15 parameters, *wR*2 = 0.0260 for HfFeGe (ZrNiAl type) and *a* = 624.10(3), *b* = 378.10(6), *c* = 725.25(7) pm, *Pnma*, 369 F^2 values, 20 parameters, *wR*2 = 0.0513 for TaFeGe (TiNiSi type). The common structural motif of the four different structures is the slightly distorted tetrahedral tetrel (*tr*) coordination of the iron atoms and a trigonal prismatic coordination of iron by *T* = Zr, Nb, Hf, Ta. Three compounds were characterized as Pauli-paramagnetic by measuring their susceptibility. The measurement of the electrical resistivity of NbFeSi characterises this compound as a good metal. Furthermore, ^{57}Fe Mössbauer spectra of all compounds could be obtained at room temperature, revealing a clear correlation between the structural distortions and the quadrupole splitting parameters.

Keywords: crystal structure; ^{57}Fe Mössbauer spectroscopy; germanides; magnetic properties; silicides.

***Corresponding author: Rainer Pöttgen,** Institut für Anorganische und Analytische Chemie, Universität Münster, Corrensstrasse 30, 48149 Münster, Germany, e-mail: pottgen@uni-muenster.de
Sebastian Stein, Theresa Block, Steffen Klenner and Lukas Heletta: Institut für Anorganische und Analytische Chemie, Universität Münster, Corrensstrasse 30, 48149 Münster, Germany

1 Introduction

Binary transition metal (*T*) silicides are technologically important and widely applied materials in thermoelectrics and microelectronic devices [1–4]. The decisive advantage of these materials relies in the large abundancy of silicon in the earth's crust as well as its low toxicity. Most prominent phases are $TiSi_2$, $TaSi_2$, $CoSi_2$, NiSi, Pd_2Si and PtSi, but several other compositions have also been thoroughly characterized.

For thermoelectrical applications, the silicides are used as bulk materials whereas thin films down to 20 nm thickness are produced for microelectronic devices. Typically, the transition metal is deposited on a silicon surface by e.g. sputtering and reacts with silicon at moderate temperature, forming the silicide. Meanwhile multilevel circuits are feasible.

Besides the binaries, over many years, phase analytical work focused on the *T*-*T*′-Si systems. Substitutions of the transition metal allow (i) for changes of the valence electron count and thus the electronic behavior and (ii) the synthesis of new ternary silicides with *T*/*T*′ ordering. One of the important families of ternary transition metal silicides concerns the equiatomic phases *TT*′Si with *T* = electron-poor and *T*′ = electron-rich transition metal. These silicides crystallize with four different structure types, TiNiSi, ZrNiAl, TiFeSi or $MgZn_2$; in the latter case with a statistical site occupancy. Also isotypic germanides have been reported. Overviews and literature surveys are given in [5–11].

The main interest in the *TT*′Si phases has concerned their superconducting behavior. However, most phases show extremely low transition temperatures. The so far highest one of 10.3 K was observed for ZrRhSi [12].

We have recently started a systematic study of the *TT*′Si phases with respect to their spectroscopic behavior [10, 13, 14]. ^{29}Si is an excellent NMR active nucleus. A systematic study of the *TT*′Si silicides revealed a clear correlation between the ^{29}Si resonance frequencies and the electronegativity of the transition metals *T* and *T*′. These results will be the subject of a separate publication.

In the present contribution we focus on the *T*FeSi silicides and their germanide counterparts. Most of these

phases were only studied on the basis of powder diffraction data [15–18]. Herein we report on crystal growth experiments and structure refinements from single crystal diffractometer data. Furthermore we studied these compounds via ^{57}Fe Mössbauer spectroscopy and magnetic susceptibility measurements.

2 Experimental

2.1 Synthesis

The iron-tetrelides *T*Fe*tr* (*T* = Zr, Nb, Hf, Ta; *tr* = Si, Ge) were synthesized directly from the elements by arc-melting. Starting materials were zirconium sponge (Johnson Matthey, 99.5%), niobium and tantalum sheets (WHS Sondermetalle, 99.5%), hafnium buttons (Smart Elements, >99.9%), iron granules (Alfa Aesar, 99.98%), silicon pieces (Merck, 99.9999%) and germanium pieces (Chempur, 99.999%) (all stated purities are metal-based). The elements were mixed in the ideal atomic ratio of *T* to Fe to *X* = 1:1:1 and were arc-melted [19] under an argon pressure of 700–800 mbar using a water-cooled copper crucible. The argon (Westfalen, 99.998%) was purified over titanium sponge (*T* = 900 K), silica gel, and molecular sieves. The ingots were turned over and re-melted several times to ensure homogeneity of the samples. Subsequently the product buttons were sealed under vacuum in silica tubes for oxidation protection and annealed at *T* = 1273–1373 K for 240 h. Afterwards the samples were quenched in ice water. The polycrystalline, air-stable compounds show metallic lustre and could be obtained phase-pure based on the X-ray powder data.

2.2 X-ray image plate data and data collection

The polycrystalline samples were characterized by powder X-ray diffraction on a Guinier camera (Enraf-Nonius FR552 equipped with a Fuji-film image plate system, BAS-1800) using Cu$K\alpha_1$ radiation and α-quartz (a = 491.30, c = 540.46 pm) as an internal standard. The lattice parameters (Table 1) were refined from the powder data. The experimental patterns were compared to calculated ones in order to ensure correct indexing [20]. We observed good agreement with the literature data.

Crystal fragments were selected from the crushed annealed ZrFeSi, NbFeGe, HfFeGe, and TaFeGe samples and glued to quartz fibers using bees wax. Their quality for intensity data collection was first checked by Laue photographs on a Buerger camera (white Mo radiation, image plate technique, Fujifilm, BAS-1800). Complete data sets were then collected either on a Stoe IPDS-II two-circle diffractometer with graphite monochromatized Mo$K\alpha$ radiation (λ = 71.073 pm) or a STOE StadiVari diffractometer equipped with a Mo micro focus source and a Pilatus detection system. Due to a Gaussian-shaped profile of the latter X-ray source, scaling was applied along with the numerical absorption correction. All relevant crystallographic data and details of the data collections and evaluations are listed in Table 2.

Table 1: Refined lattice parameters and volumes per formula unit V/Z (Guinier powder data for the present work) of the equiatomic iron tetrelides *T*Fe*X* (*T* = Zr, Nb, Hf, Ta; *X* = Si, Ge).

Compound	*a* (pm)	*b* (pm)	*c* (pm)	V/Z (nm^3)	Structure type	Reference
ZrFeSi	640.5(2)	393.5(1)	719.9(3)	0.0454	TiNiSi	[15]
ZrFeSi	640.7(1)	394.1(1)	719.1(2)	0.0454	TiNiSi	this work
NbFeSi	623.1(2)	367.7(2)	719.0(4)	0.0412	TiNiSi	[15]
NbFeSi	623.6(2)	368.2(1)	719.5(2)	0.0413	TiNiSi	this work
HfFeSi	631.9(1)	392.08(6)	714.6(1)	0.0443	TiNiSi	[16]
HfFeSi	632.5(3)	392.0(2)	715.5(3)	0.0444	TiNiSi	this work
TaFeSi	615.8(2)	371.2(1)	708.6(2)	0.0405	TiNiSi	[15]
TaFeSi	616.7(2)	371.2(1)	709.1(2)	0.0406	TiNiSi	this work
ZrFeGe	651.85(9)	389.10(5)	754.25(9)	0.0478	TiNiSi	[17]
ZrFeGe	651.4(2)	388.60(9)	754.3(2)	0.0477	TiNiSi	this work
NbFeGe	720.2(4)	1118.7(5)	650.2(3)	0.0437	TiFeSi	[18]
NbFeGe	719.4(2)	1118.9(2)	650.0(1)	0.0436	TiFeSi	this work
HfFeGe	656.6(3)	*a*	373.1(2)	0.0464	ZrNiAl	[18]
HfFeGe	657.0(1)	*a*	373.35(9)	0.0465	ZrNiAl	this work
TaFeGe	624.0(2)	378.2(1)	725.6(2)	0.0428	TiNiSi	[15]
TaFeGe	624.5(1)	378.49(9)	725.8(1)	0.0429	TiNiSi	this work

Table 2: Crystallographic data and structure refinement of ZrFeSi, NbFeGe, HfFeGe, and TaFeGe.

Empirical formula	ZrFeSi	NbFeGe	HfFeGe	TaFeGe
Formula weight, g mol^{-1}	175.2	221.3	306.9	309.4
Space group	*Pnma*	*Ima*2	$P\bar{6}2m$	*Pnma*
Formula units, *Z*	4	12	3	4
Structure type	TiNiSi	TiFeSi	ZrNiAl	TiNiSi
Lattice parameters (single crystal data)				
a, pm	640.16(3)	719.63(11)	655.96(7)	624.10(3)
b, pm	393.45(5)	1119.27(7)	*b* = *a*	378.10(6)
c, pm	718.42(6)	649.29(7)	372.54(4)	725.25(7)
Cell volume, nm^3	0.1809	0.5230	0.1388	0.1711
Calculated density, g cm^{-3}	6.43	8.43	11.01	12.01
Crystal size, μm^3	15×30×180	25×25×50	20×20×120	35×40×140
Diffractometer type	IPDS-II (STOE)	StadiVari (STOE)	IPDS-II (STOE)	StadiVari (STOE)
Detector distance, mm	70	40	70	40
Exposure time, s	120	42	180	18
ω range; step width, deg	0–180.0/1.0	−56.5 to 24.5/0.3	0–180.0/1.0	−58.0 to 24.5/0.3
Integr. param. A, B, EMS	15.0, −1.0, 0.030	7.0, −6.0, 0.030	14.0, −1.0, 0.030	7.0, −2.0, 0.030
Abs. coefficient, mm^{-1}	13.7	30.9	79.4	88.9
F(000), *e*	320	1188	390	524
θ range, deg	4–34	3–34	3–35	4–34
hkl range	±9, ±6, ±11	±11, ±17, ±9	±10, ±10, ±5	±9, ±5, ±11
Total no. reflections	4174	2164	2770	2726
Independent reflections, R_{int}	390/0.0292	1103/0.0486	251/0.0255	369/0.0308
Refl. with $I \geq 3\,\sigma(I)/R_\sigma$	336/0.0091	977/0.0256	242/0.0082	345/0.0080
Data/parameters	390/20	1103/54	251/15	369/20
Goodness-of-fit on F^2	1.02	1.31	1.03	1.94
R_1/wR_2 for $I \geq 3\,\sigma(I)$	0.0116/0.0287	0.0245/0.0549	0.0108/0.0257	0.0224/0.0510
R_1/wR_2 for all data	0.0158/0.0294	0.0282/0.0555	0.0123/0.0260	0.0241/0.0513
Extinction coefficient	131(14)	1920(90)	76(6)	241(14)
Flack parameter	–	0.41(4)	0.23(2)	–
Largest diff. peak/hole, *e* Å^{-3}	0.37/ −0.39	1.00/ −1.15	0.62/ −0.56	2.56/ −3.09

2.3 EDX data

The single crystals studied on the diffractometers (as an example we show the NbFeGe single crystal in Fig. 1) were semi-quantitatively analysed by EDX using a Zeiss EVO® MA10 scanning electron microscope in variable-pressure mode (60 Pa) with SiO_2, Fe, Zr, Nb, Ge, Hf, and Ta as internal standards. The analysis with a secondary electron detector at several points gave the experimental compositions 36±2 at.% Zr, 30±2 at.% Fe, 34±2 at.% Si (ZrFeSi crystal), 39±2 at.% Nb, 31±2 at.% Fe, 30±2 at.% Ge (NbFeGe crystal), 34±2 at.% Hf, 32±2 at.% Fe, 34±2 at.% Ge (HfFeGe crystal) and 39±2 at.% Ta, 32±2 at.% Fe, 29±2 at.% Ge (TaFeGe crystal). No impurity elements were detected.

2.4 Physical property measurements

The property measurements were carried out with a Physical Property Measurement System (QuantumDesign PPMS-9). The magnetic susceptibilities of ZrFeSi, NbFeSi and HfFeGe were measured using the VSM option with an applied magnetic field of 10 kOe (1 kOe = 7.96×10^4 A m^{-1}) in the temperature range of 3–300 K. All three

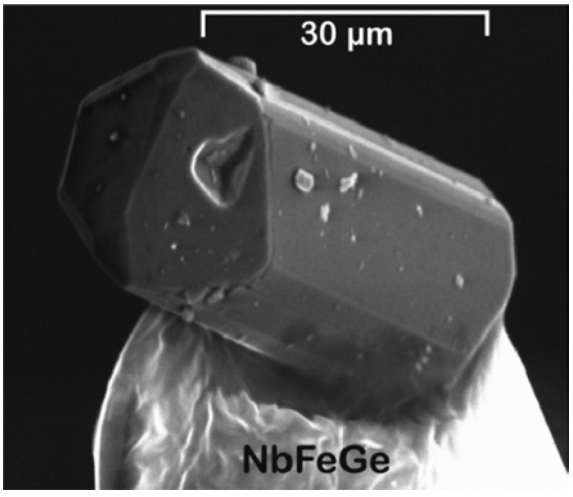

Fig. 1: Scanning electron microscopic picture (secondary electron detector) of the investigated single crystal of NbFeGe.

measurements were performed in the zero-field-cooled mode (ZFC). For NbFeSi and HfFeGe, additional measurements in field-cooled mode (FC) were carried out.

The specific electrical resistivity of NbFeSi was measured by the van der Pauw method [21] in the temperature range of 2–300 K. The previously sintered, disc shaped sample was contacted to the ac-transport puck modified by Wimbush Science and Technology with a distance of the spring probes (gold plated nickel) of 2 mm, and the applied alternate current frequency was set to 31 Hz. The maximum currents were 15 mA for the first and 20 mA for the second channel.

2.5 Mössbauer spectroscopy

For the ^{57}Fe Mössbauer-spectroscopic investigations of the *T*FeSi and *T*FeGe (*T* = Zr, Nb, Hf, Ta) samples a ^{57}Co/Rh source was used. The samples were placed in thin walled PMMA containers with an optimized thickness according to Long et al. [22]. The measurements were conducted in usual transmission geometry at room temperature with measurement periods between 1 and 6 days for each sample. To fit the spectra the routine WinNormos for Igor6 was used [23].

3 Results and discussion

3.1 Structure refinements

Isotypism of ZrFeSi and TaFeGe with the TiNiSi type (space group *Pnma*), of NbFeGe with the TiFeSi type (*Ima*2), and of HfFeGe with the ZrNiAl-type structure ($P\bar{6}2m$) was already evident from the X-ray powder data. The systematic extinctions of the data sets were compatible with these space groups. The starting atomic positions were determined using the charge-flip algorithm [24] of SuperFlip [25] and the four structures were refined on F^2 with the Jana2006 [26] software package using anisotropic displacement parameters for all atoms. All occupancy factors were refined in separate cycles leading to full occupation within two standard deviations. The final difference Fourier analyses revealed no significant residual electron densities. Refinement of the correct absolute structures of NbFeGe and HfFeGe (non-centrosymmetric space groups) was ensured through calculation of the Flack parameters [27–29].

The single crystal of NbFeGe showed pseudo-hexagonal symmetry as it was already observed by Jeitschko for the prototype TiFeSi [30, 31]. The body-centred orthorhombic lattice possesses the general reflection conditions $h+k+l=2n$; *h0l*: only $h=2n$, $l=2n$, which is compatible

Table 3: Atomic coordinates of ZrFeSi, NbFeGe, HfFeGe, and TaFeGe.

Atom	Wyck.	*x*	*y*	*z*
ZrFeSi				
Zr	4*c*	0.00537(3)	1/4	0.69479(3)
Fe	4*c*	0.15800(5)	1/4	0.06572(5)
Si	4*c*	0.2866(1)	1/4	0.39212(9)
NbFeGe				
Nb1	4*b*	1/4	0.1995(1)	0.2907(1)
Nb2	4*b*	1/4	0.7847(1)	0.2757(2)
Nb3	4*b*	1/4	0.99901(8)	0.9070(1)
Fe1	8*c*	0.0254(3)	0.37563(9)	0.1179(2)
Fe2	4*a*	0	0	0.2452(2)
Ge1	8*c*	0.0033(1)	0.16701(7)	0.9923(1)
Ge2	4*b*	1/4	0.9802(2)	0.4967(2)
HfFeGe				
Hf	3*f*	0.58293(5)	0	0
Fe	3*g*	0.2423(2)	0	1/2
Ge1	1*a*	0	0	0
Ge2	2*d*	1/3	2/3	1/2
TaFeGe				
Ta	4*c*	0.02505(6)	1/4	0.68384(4)
Fe	4*c*	0.1481(2)	1/4	0.0613(2)
Ge	4*c*	0.2677(2)	1/4	0.3779(1)

Standard deviations are given in parentheses.

Table 4: Displacement parameters (pm^2) of ZrFeSi, NbFeGe, HfFeGe, and TaFeGe.

Atom	U_{11}	U_{22}	U_{33}	U_{12}	U_{13}	U_{23}	U_{eq}
ZrFeSi							
Zr	47(1)	59(1)	58(1)	0	−7(1)	0	55(1)
Fe	51(1)	53(2)	54(1)	0	1(1)	0	53(1)
Si	46(2)	51(3)	73(3)	0	3(2)	0	57(2)
NbFeGe							
Nb1	66(4)	71(4)	52(4)	0	0	−9(3)	63(2)
Nb2	78(4)	82(4)	57(4)	0	0	12(3)	72(2)
Nb3	74(4)	67(3)	80(4)	0	0	5(3)	74(2)
Fe1	122(6)	68(4)	55(4)	3(3)	5(4)	6(4)	82(3)
Fe2	176(10)	81(6)	61(6)	−16(6)	0	0	106(4)
Ge1	66(3)	71(3)	58(3)	−5(2)	−3(3)	−1(3)	65(2)
Ge2	84(4)	99(7)	140(8)	0	0	−27(6)	107(4)
HfFeGe							
Hf	129(1)	89(1)	99(1)	45(1)	0	0	110(1)
Fe	90(3)	95(4)	184(5)	47(2)	0	0	122(3)
Ge1	189(4)	U_{11}	100(6)	95(2)	0	0	159(3)
Ge2	87(2)	U_{11}	92(4)	44(1)	0	0	89(2)
TaFeGe							
Ta	150(2)	172(2)	148(2)	0	−7(1)	0	156(1)
Fe	165(5)	156(4)	141(4)	0	5(4)	0	154(3)
Ge	159(4)	152(3)	162(4)	0	3(3)	0	158(2)

The isotropic displacement parameter U_{eq} is defined as $U_{eq} = 1/3 (U_{11} + U_{22} + U_{33})$ (pm^2). Standard deviations are given in parentheses.

Table 5: Interatomic distances (pm) in ZrFeSi, HfFeGe and TaFeGe. All distances within the first coordination spheres are listed.

ZrFeSi				HfFeGe				TaFeGe			
Zr:	2	Si	276.6	Hf:	4	Ge2	271.1	Ta:	2	Ge	266.7
	2	Si	278.5		1	Ge1	273.6		1	Ge	268.6
	2	Fe	281.5		2	Fe	290.9		2	Ge	268.8
	1	Si	282.3		4	Fe	302.2		1	Fe	284.3
	1	Fe	283.8		4	Hf	341.2		2	Fe	285.6
	1	Fe	290.6		2	Hf	372.5		2	Fe	292.0
	2	Fe	306.2						1	Fe	294.9
	1	Si	328.2						2	Ta	326.5
	2	Zr	329.8						2	Ta	328.4
	2	Zr	342.2						1	Ge	356.1
Fe:	2	Si	235.6	Fe:	2	Ge1	244.9	Fe:	2	Ge	237.0
	1	Si	239.7		2	Ge2	253.8		1	Ge	241.5
	1	Si	248.5		2	Fe	275.3		1	Ge	241.5
	2	Zr	281.5		2	Hf	290.9		2	Fe	278.9
	1	Zr	283.8		4	Hf	302.2		1	Ta	284.3
	1	Zr	290.6						2	Ta	285.6
	2	Fe	297.6						2	Ta	292.0
	2	Zr	306.2						1	Ta	294.9
Si:	2	Fe	235.6	Ge1:	6	Fe	244.9	Ge:	2	Fe	237.0
	1	Fe	239.7		3	Hf	273.6		1	Fe	241.5
	1	Fe	248.5	Ge2:	3	Fe	253.8		1	Fe	241.5
	2	Zr	276.6		6	Hf	271.1		2	Ta	266.7
	2	Zr	278.5						1	Ta	268.6
	1	Zr	282.3						2	Ta	268.8

Standard deviations are all smaller or equal to 0.3 pm.

with the space group *Ima*2 (no. 46). The formation of trillings is observed due to the *translationsgleiche* symmetry reduction of index 3 (*t*3) from space group $P\bar{6}2m$ of the aristotype Fe_2P into the orthohexagonal setting [32]. The trilling formation can be described by the following matrices:

$$M_2 = \begin{pmatrix} 1 & 0 & 0 \\ 0 & -\frac{1}{2} & \frac{3}{2} \\ 0 & -\frac{1}{2} & -\frac{1}{2} \end{pmatrix}; \qquad M_3 = \begin{pmatrix} 1 & 0 & 0 \\ 0 & -\frac{1}{2} & -\frac{3}{2} \\ 0 & \frac{1}{2} & -\frac{1}{2} \end{pmatrix}$$

The trilling domain ratios were refined separately, leading to an amount of M_1:M_2≈9:1 and a negligible contribution of the third domain (M_3≈0).

All positional parameters and interatomic distances are listed in Tables 3–6.

CCDC 1877715 (ZrFeSi), 1877716 (NbFeGe), 1877718 (HfFeGe) and 1877719 (TaFeGe) contain the supplementary crystallographic data for this paper. These data can be obtained free of charge from The Cambridge Crystallographic Data Centre via www.ccdc.cam.ac.uk/data_request/cif.

Table 6: Interatomic distances (pm) in NbFeGe. All distances within the first coordination spheres are listed.

Nb1:	2	Ge1	265.3	Fe1:	1	Ge2	241.6
	2	Ge1	266.4		1	Ge2	243.2
	2	Fe1	278.5		1	Ge1	247.8
	1	Ge1	279.6		1	Ge1	248.2
	2	Fe1	279.9		1	Nb1	278.5
	2	Fe2	288.3		1	Fe2	279.8
	1	Nb3	335.3		1	Nb1	279.9
	2	Nb1	343.8		1	Fe1	280.8
	1	Nb3	345.8		1	Nb3	284.7
Nb2:	1	Ge2	261.7		1	Nb2	286.3
	2	Ge1	264.6	Fe2:	2	Ge2	244.0
	2	Ge1	265.2		2	Ge1	248.8
	2	Fe1	286.3		2	Fe1	279.8
	2	Fe2	301.4		2	Nb3	283.9
	2	Fe1	314.7		2	Nb1	288.3
	1	Nb3	328.7		2	Nb2	301.4
	2	Nb2	333.8	Ge1:	1	Fe1	247.8
	1	Nb3	338.9		1	Fe1	248.2
Nb3:	2	Ge1	264.5		1	Fe2	248.8
	2	Ge1	266.1		1	Nb3	264.5
	1	Ge2	267.2		1	Nb2	264.6
	2	Fe2	283.9		1	Nb2	265.2
	2	Fe1	284.7		1	Nb1	265.3
	2	Fe1	305.9		1	Nb3	266.1
	1	Nb2	328.7		1	Nb1	266.4
	1	Nb1	335.3	Ge2:	2	Fe1	241.6
	1	Nb2	338.9		2	Fe1	243.2
	1	Nb1	345.8		2	Fe2	244.0
					1	Nb2	261.7
					1	Nb3	267.2
					1	Nb1	279.6

Standard deviations are all smaller or equal to 0.3 pm.

3.2 Crystal chemistry

In the present study we have investigated eight iron-based equiatomic silicides *T*FeSi and germanides *T*FeGe with *T* = Zr, Nb, Hf and Ta. Although the main focus on these phases lies in the ^{57}Fe Mössbauer-spectroscopic study (*vide infra*), we also characterized the samples through powder X-ray diffraction and additionally refined four structures from single crystal diffractometer data. Our data fully confirm the original literature. In that context, it is interesting to note, that a recent theoretical investigation [33] claimed the cubic half-Heusler phase structure for ZrFeSi. Our single crystal data, however, undoubtedly prove that ZrFeSi has the orthorhombic TiNiSi-type structure. The total energy calculations thus do not reproduce the ground state under ambient conditions correctly. In addition, the calculated cell volume of 0.0498 nm^3 per formula unit is significantly higher (ca. 10%) than the value of 0.0454 nm^3

determined in the present work. Keeping the small volume changes during phase transitions for such intermetallics in mind (typical examples are ErAgSn [34] or ScRuSi [35]), the theoretical results are highly questionable.

In the following discussion, we only briefly focus on the crystal chemical details, since these tetrelides crystallize in well-known prototypes [36]. Furthermore, we focus on the respective iron coordination, which is relevant for the discussion of the ^{57}Fe Mössbauer-spectroscopic data (*vide infra*). ZrFeSi, NbFeSi, HfFeSi, TaFeSi, ZrFeGe, and TaFeGe crystallize with the TiNiSi-type structure [37], space group *Pnma*. As an example, we present the iron coordination of ZrFeSi in Fig. 2. The structure contains only one crystallographic iron site, and each iron atom shows distorted tetrahedral silicon coordination with Fe–Si distances ranging from 236 to 249 pm. At least the shorter ones are close to the sum of the covalent radii for Fe + Si of 233 pm [38]. Substantially distorted trigonal prisms of zirconium atoms surround the $FeSi_4$ tetrahedra.

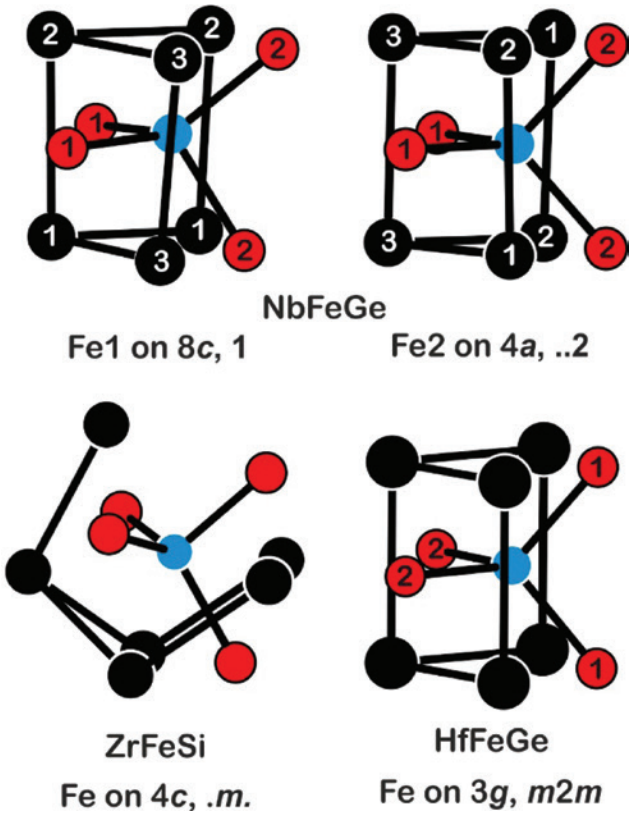

Fig. 2: Coordination of the iron atoms in the structures of NbFeGe, ZrFeSi and HfFeGe. The Wyckoff positions, the site symmetries, and the crystallographically independent sites are indicated. Zirconium (hafnium, tantalum), iron and silicon (germanium) atoms are drawn as black, blue and red circles, respectively.

HfFeGe adopts the ZrNiAl type [39–41], space group $P\bar{6}2m$. This structure also contains only one iron site; again with tetrahedral germanium coordination. The Fe–Ge distances of 245 and 254 pm are slightly longer than the sum of the covalent radii for Fe + Ge of 238 pm [38]. This bonding situation is similar to that of ZrFeSi discussed above. In contrast to the silicide, we observe a symmetrical trigonal Hf_6 prism around the $FeGe_4$ tetrahedron.

The corresponding niobium compound NbFeGe is structurally closely related to HfFeGe, however, we observe a small structural distortion. If the sizes of the three elements forming a ZrNiAl related compound do not exactly match, puckering of the atoms (and this is not necessarily a function of the electron count) leads to superstructure formation [42, 43]. However, of the more than 1000 ZrNiAl related phases [11] only 11 were ascribed to the HfRhSn-type superstructure, space group $P\bar{6}2c$ [11, 42] and 38 to the TiFeSi-type superstructure, space group *Ima*2 [11, 31]. NbFeGe adopts the latter ordering variant. So far, only the prototype itself and the isotypic stannide ScAgSn [44] were studied on the basis of single crystal diffraction data. The group-subgroup relation has been discussed for ScAgSn. The first *translationengleiche* symmetry reduction induces the formation of trillings. In the TiFeSi-type superstructure the iron site splits into two crystallographically independent sites 8*c* and 4*a* with individual distortions. This is readily evident from the different Fe–Ge distances within the $FeGe_4$ tetrahedra with slightly shorter ones for Fe1 (Table 6).

The three different structures do not only have the tetrahedral tetrel coordination of the iron atoms in common. We also observe weak Fe–Fe contacts for all four compounds studied. Each iron atom has two closer iron neighbors at Fe–Fe distances ranging from 275 to 298 pm, distinctly longer than in *bcc* iron, where each iron atoms has eight neighbors at 248 pm [45].

3.3 Magnetic properties of ZrFeSi, NbFeSi and HfFeGe

The temperature dependence of the magnetic susceptibility of ZrFeSi, NbFeSi and HfFeGe is presented in Fig. 3. The three compounds show almost temperature-independent Pauli-paramagnetic behavior due to substantial contributions from the conduction electrons, over-compensating the intrinsic diamagnetism. The measured molar susceptibilities at $T = 300$ K are $4.15(2) \times 10^{-4}$ (ZrFeSi), $12.0(1) \times 10^{-4}$ (NbFeSi) and $8.63(2) \times 10^{-4}$ emu mol^{-1} (HfFeGe). The slight increases of χ below 50–100 K are due to small amounts of paramagnetic impurities (Curie tails). Since the FC and ZFC measurement curves of NbFeSi and HfFeGe are

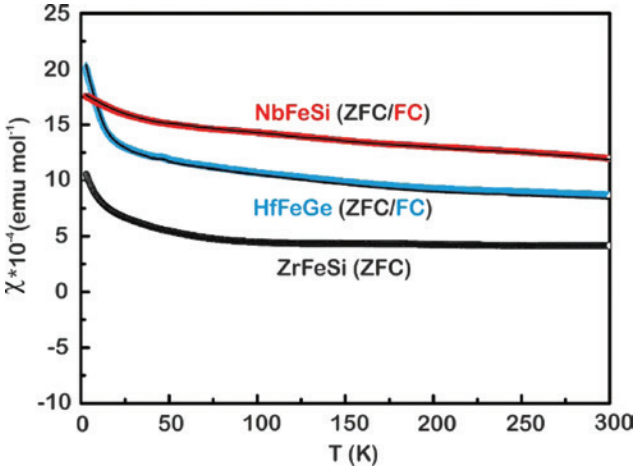

Fig. 3: Temperature dependences of the molar magnetic susceptibility of ZrFeSi (black), NbFeSi (red) and HfFeGe (blue) at an external magnetic field strength of 10 kOe in the temperature range of 3–300 K.

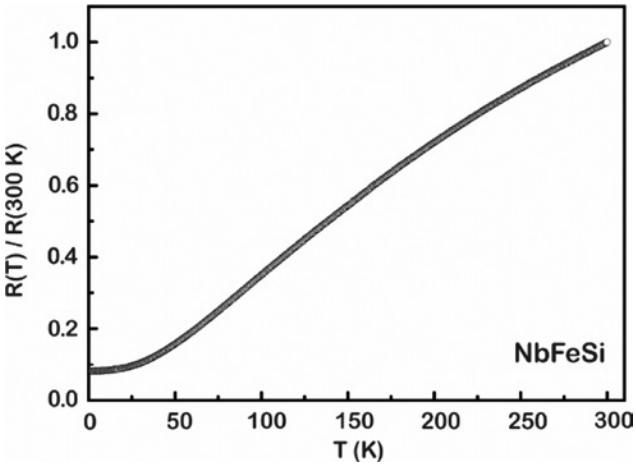

Fig. 4: Reduced electrical resistivity $R(T)/R(300\ K)$ of NbFeSi measured in the temperature range 2–300 K.

superimposed, we can rule out ferromagnetic interactions caused by iron particles at the grain boundaries.

Again we compare our experimental data for ZrFeSi with electronic-structure calculations [33]. The band structure analyses revealed high spin polarization for ZrFeSi in a half-Heusler-type structure. This finding also contradicts the Pauli paramagnetism correctly determined in the present work.

3.4 Electrical properties of NbFeSi

The reduced resistivity $R(T)/R(300\ K)$ of NbFeSi measured in the range 2–300 K is presented in Fig. 4. The resistivity decreases with decreasing temperature. Down to ca. 50 K the decrease is almost linear, while we observe proportionality to ~ T^5 in the 2–50 K regime, in agreement with Bloch's theory (increasing electron phonon coupling with increasing temperature). At $T = 2$ K the residual-resistivity ratio (RRR, defined as $R(300\ K)/R(T)$) is 12.2, classifying NbFeSi as a good metal.

3.5 ^{57}Fe Mössbauer spectroscopy

Figure 5 shows the ^{57}Fe Mössbauer spectra of the equiatomic iron-tetrelides *T*Fe*X* (*T* = Zr, Nb, Hf, Ta; *X* = Si, Ge) at room temperature along with transmission integral fits. The underlying fitting parameters are listed in Table 7. Although the eight tetrelides crystallize with three different structure types, the tetrahedral tetrel coordination of the iron atoms is their common structural motif. Thus, we have a small model system to systematically study small changes in the iron coordination by ^{57}Fe Mössbauer spectroscopy.

In the following we discuss the isomer shift values which are a measure for the electron density at the iron nuclei, and the quadrupole splitting (ΔE_Q) values which reflect the degree of asymmetry of the iron coordination. The isomer shifts vary from ca. 0 mm s^{-1} for most TiNiSi-type compounds to ca. 0.2 mm s^{-1} for the ZrNiAl type germanides, indicating higher electron density at the iron nuclei in the latter [46, 47]. However, the isomer shifts show no direct correlation with the electron count, most likely due to small differences induced by the different structure types.

A readily visible difference concerns the quadrupole splitting parameters which cover the broad range from 0.142 to 0.693 mm s^{-1} (Table 7). We can relate these differences with the Fe*tr*$_4$ tetrahedra and first focus on the structures of ZrFeSi, HfFeGe and TaFeGe refined in the present work. The Fe–Ge distances in TaFeGe (237 and 242 pm) and HfFeGe (245 and 254 pm) show small ranges and this is directly expressed in quadrupole splitting parameters of 0.204 mm s^{-1} for HfFeGe and 0.306 mm s^{-1} for TaFeGe. The asymmetry of the iron coordination is caused by the differences in the Fe–Ge distances, the Ge–Fe–Ge bond angles and the hafnium, respectively tantalum coordination around the tetrahedra. The latter is much more asymmetric in TiNiSi-type TaFeGe (compare the distorted trigonal prism of ZrFeSi shown in Fig. 2) than in HfFeGe which has a regular polyhedron, explaining the higher ΔE_Q value for TaFeGe.

As a second example, we compare the isotypic structures of TaFeGe and ZrFeSi. The iron atoms in the silicide

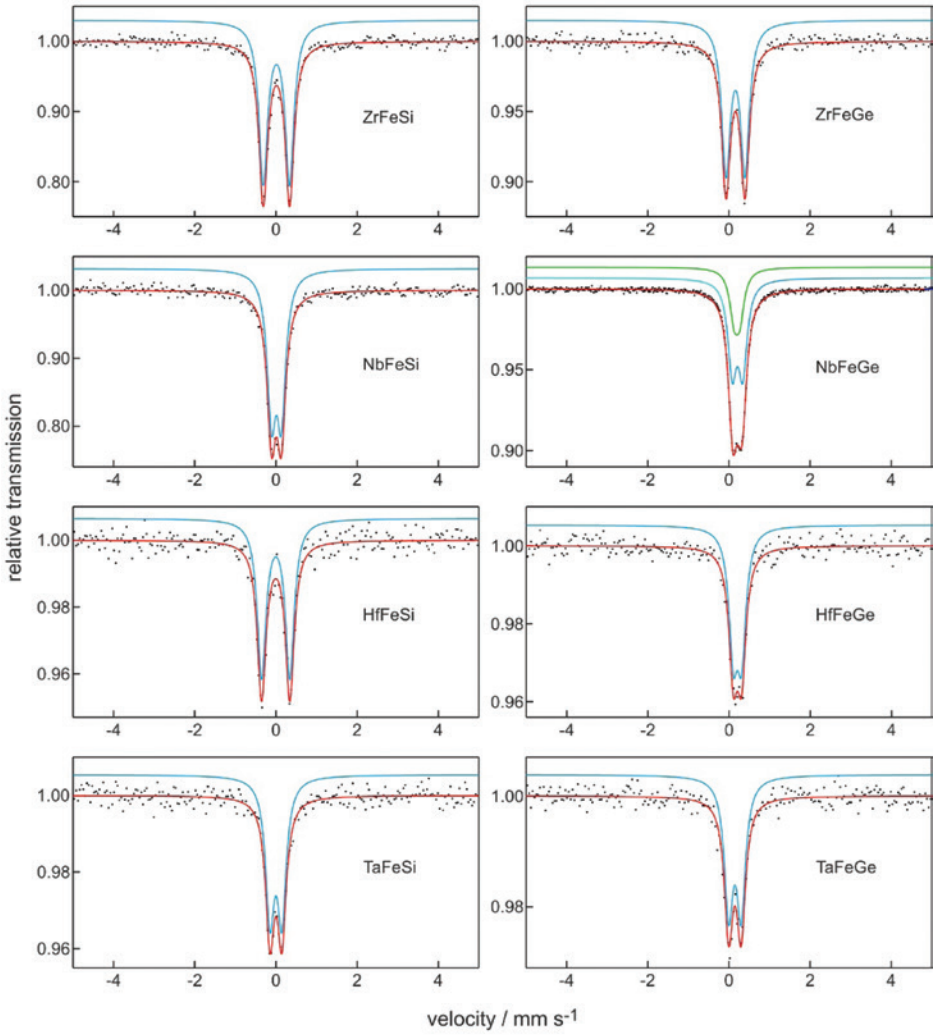

Fig. 5: ^{57}Fe Mössbauer spectra of the tetrelides *T*FeSi and *T*FeGe (*T* = Zr, Nb, Hf, Ta) at room temperature.

Table 7: Fitting parameters for the ^{57}Fe Mössbauer spectroscopic results of the tetrelides *T*FeSi and *T*FeGe (*T* = Zr, Nb, Hf, Ta) at room temperature; δ = isomer shift, ΔE_Q = electric quadrupole splitting, Γ = experimental line width.

Compound	δ (mm · s^{-1})	ΔE_Q (mm · s^{-1})	Γ (mm · s^{-1})	Ratio
ZrFeSi	0.013(1)	0.648(3)	0.26*	100
NbFeSi	0.011(2)	0.241(3)	0.26*	100
HfFeSi	−0.005(3)	0.693(6)	0.26*	100
TaFeSi	−0.001(4)	0.290(6)	0.26*	100
ZrFeGe	0.160(2)	0.466(3)	0.26*	100
NbFeGe				
(blue)	0.210(1)	0.257(2)	0.26*	67*
(green)	0.195(2)	0.142(5)	0.26*	33*
HfFeGe	0.204(4)	0.204(7)	0.26*	100
TaFeGe	0.146(4)	0.306(6)	0.26*	100

Parameters marked with an asterisk were kept fixed during the fitting procedure.

have 3+1 tetrahedral silicon coordination with three closer Fe–Si distances of 2×236 and 1×240 and a fourth one at 249 pm. TaFeGe shows a much smaller range with 2×237, 1×241 and 1×241 pm. This leads to a significantly higher quadrupole splitting parameter of 0.648 mm s^{-1} for ZrFeSi. An even higher ΔE_Q value of 0.693 mm s^{-1} has been refined for HfFeSi and we can expect a similar structural distortion for the $FeSi_4$ tetrahedra in this silicide.

Finally, we turn to the NbFeGe superstructure. The symmetry reduction leads to a 2:1 splitting of the subcell iron site to Fe1 on 8*c* and Fe2 on 4*a*. The NbFeGe spectrum shows a slightly broader signal because of the superposition of two separate sub-signals. The spectrum could be reproduced by two signals in an intensity ratio of 2 to 1 of which the blue one (for Fe1 on 8*c*) shows a slightly higher quadrupole splitting. This is consistent with the course of the interatomic distances, i.e. a slightly more asymmetric

1:1:1:1 coordination for Fe1 and a 2:2 coordination for Fe2 (Table 6).

Summing up, we observed well-resolved ^{57}Fe Mössbauer spectra for the series of *T*Fe*X* (*T* = Zr, Nb, Hf, Ta; *X* = Si, Ge) tetrelides. The small structural distortions within and around the different Fe*tr*$_4$ tetrahedra are directly expressed in the ^{57}Fe spectra. Thus, ^{57}Fe Mössbauer spectroscopy is a suitable complementary tool for structure elucidation of intermetallic iron compounds.

Acknowledgements: We thank Dr. Rolf-Dieter Hoffmann and Dipl.-Ing. Jutta Kösters for collecting the single-crystal intensity data.

References

[1] L. Miglio, F. d'Heurle (Eds.), *Silicides – Fundamentals and Applications*, World Scientific, Singapore, **2000**.
[2] S.-L. Zhang, M. Östling, *Crit. Rev. Solid State Mater. Sci*. **2003**, *28*, 1.
[3] L. J. Chen, *JOM* **2005**, *57*, 24.
[4] A. Nozariasbmarz, A. Agarwal, Z. A. Coutant, M. J. Hall, J. Liu, R. Liu, A. Malhotra, P. Norouzzadeh, M. C. Öztürk, V. P. Ramesh, Y. Sargolzaeiaval, F. Suarez, D. Vashaee, *Jpn. J. Appl. Phys*. **2017**, *56*, 05DA04.
[5] H. Barz, H. C. Ku, G. P. Meisner, Z. Fisk, B. T. Matthias, *Proc. Natl. Acad. Sci*. **1980**, *77*, 3132.
[6] R. Müller, R. N. Shelton, J. W. Richardson, Jr., R. A. Jacobson, *J. Less-Common Met*. **1983**, *92*, 177.
[7] S. Yashiro, A. Kasahi, R. Kasai, H. Samata, Y. Nagata, *J. Alloys Compds*. **2000**, *309*, 51.
[8] R. Mishra, R. Pöttgen, G. Kotzyba, *Z. Naturforsch*. **2001**, *56b*, 463.
[9] T. Dinges, M. Eul, R. Pöttgen, *Z. Naturforsch*. **2010**, *65b*, 95.
[10] C. Benndorf, L. Heletta, G. Heymann, H. Huppertz, H. Eckert, R. Pöttgen, *Solid State Sci*. **2017**, *68*, 32.
[11] P. Villars, K. Cenzual, *Pearson's Crystal Data: Crystal Structure Database for Inorganic Compounds* (release 2017/18), ASM International®, Materials Park, Ohio (USA), **2017**.
[12] I. Shirotani, Y. Konno, Y. Okada, Ch. Sekine, S. Todo, T. Yagi, *Solid State Commun*. **1998**, *108*, 967.
[13] C. Benndorf, *Multinukleare Festkörper NMR spektroskopische Untersuchungen ausgewählter intermetallischer Verbindungen*, Dissertation, Universität Münster, Münster, **2016**.
[14] C. Benndorf, H. Eckert, R. Pöttgen, *Dalton Trans*. **2016**, *45*, 8215.
[15] W. Jeitschko, A. G. Jordan, P. A. Beck, *Trans. Metall. Soc. AIME* **1969**, *245*, 335.
[16] J. T. Zhao, E. Parthé, *J. Less-Common Met*. **1990**, *163*, L7.
[17] V. Johnson, W. Jeitschko, *J. Solid State Chem*. **1972**, *4*, 123.
[18] W. Jeitschko, *Metall. Trans*. **1970**, *1*, 2963.
[19] R. Pöttgen, T. Gulden, A. Simon, *GIT Labor-Fachzeitschrift* **1999**, *43*, 133.
[20] K. Yvon, W. Jeitschko, E. Parthé, *J. Appl. Crystallogr*. **1977**, *10*, 73.
[21] L. J. van der Pauw, *Philips Res. Rep*. **1958**, *13*, 1.
[22] G. J. Long, T. E. Cranshaw, G. Longworth, *Moessbauer Eff. Ref. Data J*. **1983**, *6*, 42.
[23] R. A. Brand, WinNormos for Igor6, version for Igor 6.2 or above: 22.02.2017, Universität Duisburg, Duisburg, Germany, **2017**.
[24] L. Palatinus, *Acta Crystallogr*. **2013**, *B69*, 1.
[25] L. Palatinus, G. Chapuis, *J. Appl. Crystallogr*. **2007**, *40*, 786.
[26] V. Petříček, M. Dušek, L. Palatinus, *Z. Kristallogr*. **2014**, *229*, 345.
[27] H. D. Flack, G. Bernadinelli, *Acta Crystallogr*. **1999**, *A55*, 908.
[28] H. D. Flack, G. Bernadinelli, *J. Appl. Crystallogr*. **2000**, *33*, 1143.
[29] S. Parsons, H. D. Flack, T. Wagner, *Acta Crystallogr*. **2013**, *B69*, 249.
[30] W. Jeitschko, *Acta Crystallogr*. **1969**, *A25*, S97.
[31] W. Jeitschko, *Acta Crystallogr*. **1970**, *B26*, 815.
[32] H. Wondratschek, U. Müller (Eds.), *International Tables for Crystallography*, Vol. A1, Symmetry relations between space groups, 2nd edition, John Wiley & sons, Ltd, Chichester, **2010**.
[33] S. Yousuf, D. C. Gupta, *Phys. B: Condens. Matter* **2018**, *534*, 5.
[34] C. P. Sebastian, G. Heymann, B. Heying, U. Ch. Rodewald, H. Huppertz, R. Pöttgen, *Z. Anorg. Allg. Chem*. **2007**, *633*, 1551.
[35] R.-D. Hoffmann, U. Ch. Rodewald, S. Haverkamp, C. Benndorf, H. Eckert, B. Heying, R. Pöttgen, *Solid State Sci*. **2017**, *72*, 109.
[36] E. Parthé, L. Gelato, B. Chabot, M. Penzo, K. Cenzual and R. Gladyshevskii, TYPIX–*Standardized Data and Crystal Chemical Characterization of Inorganic Structure Types*, *Gmelin Handbook of Inorganic and Organometallic Chemistry*, 8th edition, Springer, Berlin, **1993**.
[37] C. B. Shoemaker, D. P. Shoemaker, *Acta Crystallogr*. **1965**, *18*, 900.
[38] J. Emsley, *The Elements*, Oxford University Press, Oxford, **1999**.
[39] P. I. Krypyakevich, V. Ya. Markiv, E. V. Melnyk, *Dopov. Akad. Nauk. Ukr. RSR, Ser. A* **1967**, 750.
[40] A. E. Dwight, M. H. Mueller, R. A. Conner, Jr., J. W. Downey, H. Knott, *Trans. Met. Soc. AIME* **1968**, *242*, 2075.
[41] M. F. Zumdick, R.-D. Hoffmann, R. Pöttgen, *Z. Naturforsch*. **1999**, *54b*, 45.
[42] M. F. Zumdick, R. Pöttgen, *Z. Kristallogr*. **1999**, *214*, 90.
[43] R. Pöttgen, *Z. Anorg. Allg. Chem*. **2014**, *640*, 869.
[44] C. P. Sebastian, L. Zhang, C. Fehse, R.-D. Hoffmann, H. Eckert, R. Pöttgen, *Inorg. Chem. 46*, **2007**, 771.
[45] J. Donohue, *The Structures of the Elements*, Wiley, New York, **1974**.
[46] B. Fultz, *Mössbauer Spectroscopy* in *Characterization of Materials*, (Ed.: E. Kaufman), J. Wiley, New York, **2011**.
[47] F. E. Wagner, *Mössbauerspektroskopie*, in *Untersuchungsmethoden in der Chemie*, (Hrsg.: H. Naumer, W. Heller), 2. Auflage, Georg Thieme Verlag, Stuttgart, Kapitel 16, **1990**.